













ALMA observation of evolving magnetized corona in the radio-quiet changing-state AGN NGC 1566

Arghajit Jana¹ *, Claudio Ricci^{1,2} , Sophie M. Venselaar¹ , Chin-Shin Chang³ , Mai Liao¹ ,
Yoshiyuki Inoue^{4,5,6} , Taiki Kawamuro^{4,7} , Franz E. Bauer⁸ , Elena Shablovinskaya¹ ,
Benny Trakhtenbrot¹⁰ , Jacob S. Elford¹ , Michael J. Koss^{11,9} 

¹Instituto de Estudios Astrofísicos, Facultad de Ingeniería y Ciencias, Universidad Diego Portales, Av. Ejército Libertador 441, Santiago, Chile

²Kavli Institute for Astronomy and Astrophysics, Peking University, Beijing 100871, People's Republic of China

³Joint ALMA Observatory, Avenida Alonso de Cordova 3107, Vitacura 7630355, Santiago, Chile

⁴Department of Earth and Space Science, Graduate School of Science, Osaka University, 1-1 Machikaneyama, Toyonaka, Osaka 560-0043, Japan

⁵Interdisciplinary Theoretical & Mathematical Science Program (iTHEMS), RIKEN, 2-1 Hirosawa, 351-0198, Japan

⁶Kavli Institute for the Physics and Mathematics of the Universe (WPI), UTIAS, The University of Tokyo, 5-1-5 Kashiwanoha, Kashiwa, Chiba 277-8583, Japan

⁷RIKEN Cluster for Pioneering Research, 2-1 Hirosawa, Wako, Saitama, Saitama 351-0198, Japan

⁸Instituto de Alta Investigación, Universidad de Tarapacá, Casilla 7D, Arica, Chile

⁹Space Science Institute, 4750 Walnut Street, Suite 205, Boulder, Colorado 80301, USA

¹⁰School of Physics and Astronomy, Tel Aviv University, Tel Aviv 69978, Israel

¹¹Eureka Scientific, 2452 Delmer Street Suite 100, Oakland, CA 94602-3017, USA

Accepted XXX. Received YYY; in original form ZZZ

ABSTRACT

The origin of compact millimeter (mm) continuum emission from radio-quiet AGNs (RQAGNs) is still not fully understood. Changing-state AGNs (CSAGNs) display rapid and strong variability, which can allow us to investigate the origin of the mm emission. We present here the results of the first study of the mm continuum variability of a CSAGN using archival ALMA band 6 (~ 230 GHz) observations of NGC 1566 obtained in 2014–2023. We find a positive correlation between the mm and X-ray flux with an intrinsic scatter of 0.05 dex (1σ), suggesting a common origin. The mm spectral index (α_{mm}) is found in the range of 0.13 ± 0.38 to -0.26 ± 0.53 , consistent with a compact optically thick synchrotron source. No significant correlation was found between the α_{mm} and the mm flux. The mm/X-ray ratio also shows no clear link to the Eddington ratio but is higher in the low-accretion state. We discuss several scenarios about the origin of the mm emission in NGC 1566. We find that synchrotron emission in the magnetized X-ray corona appears to be the most probable origin of mm emission, confirming that mm emission can be used as a tracer of AGN activity in RQAGNs.

Key words. Galaxies: active – Galaxies: nuclei – quasars: supermassive black holes – X-rays: galaxies – Submillimeter: galaxies – Accretion, accretion disks

1. Introduction

Active galactic nuclei (AGNs), powered by accretion onto supermassive black holes (SMBHs), are classified as radio-loud (RL) or radio-quiet (RQ) based on their radio emission (Begelman et al. 1984; Wilson & Colbert 1995). RL AGNs exhibit strong jet-driven radio emission, while RQAGNs show weaker compact, unresolved nuclear radio sources, potentially arising from processes such as outflows, compact jets, X-ray coronae, or star formation (SF; e.g., Padovani 2017; Panessa et al. 2019). Among these, the synchrotron emission from a magnetized X-ray corona as a source of radio emission is particularly intriguing (Field & Rogers 1993; Inoue & Doi 2018), as it may also explain the heating mechanisms of the corona, which remain debated (e.g., Beloborodov 2017, but see also Inoue et al. 2024; Hopkins 2024).

The X-ray corona is a compact region of hot electron plasma near the SMBH, where UV seed photons are Compton up-scattered to produce X-rays (Fabian et al. 2015; Haardt & Maraschi 1993; Chakrabarti & Titarchuk 1995). Magnetic reconnection is believed to be responsible for the coronal heating (Di Matteo et al. 1997; Merloni & Fabian 2001; Cheng et al. 2020), and such a magnetized corona would emit synchrotron radiation detectable in the millimeter (mm) regime (Di Matteo et al. 1997; Laor & Behar 2008; Inoue & Doi 2014). Theoretical models predict that the synchrotron emission would peak around ~ 100 GHz and extend up to ~ 300 GHz with a flat spectrum due to synchrotron self absorption (SSA; Inoue & Doi 2014; Rąginski & Laor 2016; del Palacio et al. 2025). If the mm emission originates in the corona, we expect it to correlate with X-ray emission strongly.

Behar et al. (2015) found a possible mm/X-ray correlation in a sample of eight RQAGNs, though this corre-

* E-mail: arghajit.jana@mail.udp.cl

lation weakened in a larger sample of 34 sources with a large scatter of ~ 0.5 dex (Behar et al. 2018). Kawamuro et al. (2022) observed a significant correlation between X-ray and 230 GHz emission while studying a sample of 98 AGNs with an intrinsic scatter of ~ 0.34 dex. Ricci et al. (2023) found a tight correlation between X-ray and 100 GHz emission with an intrinsic scatter of ~ 0.22 dex using high resolution ALMA data. To date, only a few studies have investigated the simultaneous mm/X-ray variability, revealing significant mm emission variability on a timescale of days (Baldi et al. 2015; Behar et al. 2020; Petrucci et al. 2023; Shablovinskaya et al. 2024). In NGC 7469, the mm emission varied by a factor of ~ 2 over ~ 4 -5 days, while MCG +08-11-11 showed intra-day mm variability (Petrucci et al. 2023). Additionally, Shablovinskaya et al. (2024) found that the mm emission in IC 4329A changed by a factor of ~ 3 within four days, exceeding the variability of X-rays in the same timescale (see also Michiyama et al. 2024, for the case of GRS 1734-292).

Changing-look AGNs (CLAGNs) switch between type 1 and type 2 states, with the appearance and disappearance of broad emission lines in the UV/optical spectra on a timescale of months to years (see Ricci & Trakhtenbrot 2023 for a recent review). These optical state transitions are mainly driven by changes in the accretion rate, and these CLAGNs are referred as changing-state AGNs (Stern et al. 2018; Ricci & Trakhtenbrot 2023; Temple et al. 2023; Jana et al. 2025). The CS transitions are often accompanied by multi-wavelength variability, including UV, optical, IR, and X-ray bands (MacLeod et al. 2016; Noda & Done 2018; Zeltyn et al. 2024).

The change of the accretion rate could occur in two possible ways: i) disk perturbations caused, for example, by a tidal disruption event (Merloni et al. 2015; Trakhtenbrot et al. 2019; Ricci et al. 2020); ii) local disk instabilities (Stern et al. 2018; Noda & Done 2018). The latter scenario seems to be the most common (e.g., Ricci & Trakhtenbrot 2023; Jana et al. 2025), and during these CS transitions, the geometry of the inner accretion flow is also expected to change (Noda & Done 2018; Ruan et al. 2019). In the type 1 state, the disk extends to the inner most stable circular orbit, while, in the type 2 state, the disk recedes, whereby the inner accretion disk is replaced by a radiatively inefficient accretion flow (RIAF) or an extended X-ray corona (Chakrabarti & Titarchuk 1995; Reis & Miller 2013; Yuan & Narayan 2014).

During the CS transitions, the physical properties of the X-ray corona, such as its geometry, temperature, and electron density, are expected to evolve (Noda & Done 2018; Ruan et al. 2019). If mm emission originates from the corona, it too may vary as the AGN changes spectral state. Therefore, CSAGNs provide a unique opportunity to investigate the origin of the mm emission and its relation with the accretion state.

NGC 1566, a nearby ($z=0.005$) CSAGN, located at a distance of 17.9 Mpc (Koss et al. 2022), is an ideal source to investigate the origin of mm emission variability. This source has shown rapid multi-wavelength variability over decades (Alloin et al. 1986; Baribaud et al. 1992). In 2018, it underwent an outburst, transitioning to a type 1 state with the appearance of broad optical lines, before fading back to a type 2 state in 2020 (Oknyansky et al. 2021; Ochmann et al. 2024).

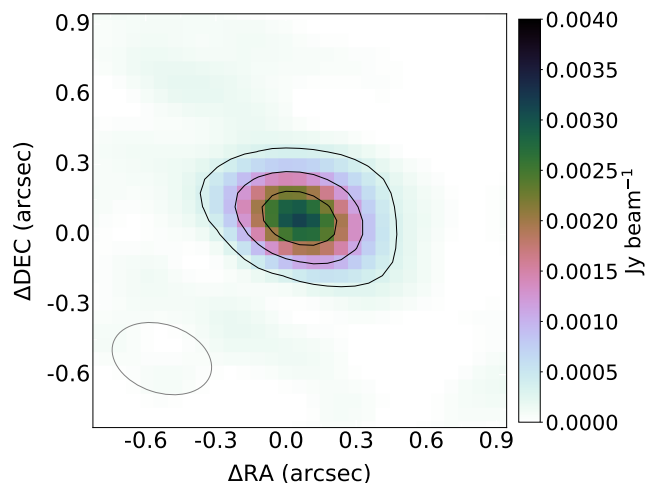


Fig. 1. ALMA image of NGC 1566 in band 6 at 230 GHz, observed on 2022-06-14. The synthesized beam size (gray ellipse at the lower corner) is $0''.44 \times 0''.29$ (38×25 pc). The contours of the emission are drawn at $(3, 10, 20)\sigma$, where $\sigma = 0.1$ mJy beam $^{-1}$. For NGC 1566, 1 arcsec angular width corresponds to 87 pc in physical scale.

NGC 1566 was observed in radio band (~ 1.4 GHz) in the past by ASKAP and ATCA, but at relatively in low resolution (with beam size $\sim 42'' \times 35''$; e.g., Ehle et al. 1996; Elagali et al. 2019). However, these observations are not relevant to studying the nuclear mm emission. In this work, we present the first study of mm and X-ray variability in a CSAGN, NGC 1566, using archival high resolution ALMA Band 6 (~ 230 GHz) data spanning between 2014 and 2023. We investigate the variability and origin of the mm emission and its relation to the accretion state.

The paper is organized in the following way. In Section 2, we present the data analysis process. In Section 3, we present our results and discuss our findings. Finally, in Section 4, we summarize our results. Throughout the paper, we adopt Λ -CDM cosmology with $H_0 = 70$ km s $^{-1}$ Mpc $^{-1}$, $\Omega_m = 0.3$ and $\Omega_\Lambda = 0.7$. At $z=0.005$, this cosmology implies an angular scale of 0.087 kpc/arcsec.

2. Observation and data analysis

ALMA observed NGC 1566 in Band 6 (230 GHz) across eight epochs between 2014 and 2023. The data were processed using CASA version 6.5.4.9 and the ALMA Pipeline version 2020.1.0.40 (Hunter et al. 2023, please see Section C for details of ALMA data analysis). For our analysis, we only considered the channels with continuum emissions for. The central source was detected at various significance levels, with a signal-to-noise ratio ranging from 100 to 700, with a position consistent with the nominal nucleus of the galaxy. Based on a Gaussian 2D fit, the central emission appears unresolved at all resolutions probed (beam sizes ranging from $0.2''$ to $7.3''$, corresponding to physical scales of $\sim 20 - 640$ pc). We have included an error of 10% in all data, as recommended in the ALMA proposer's guide. An in-band spectral index (α_{mm}) was derived from flux measurements in four spectral windows, following $F_\nu \propto \nu^{\alpha_{\text{mm}}}$. Details of the observations are summarized in Table A.1. Figure 1 shows the ALMA band 6 image of the source, obtained on June 14, 2022.

The 14 – 150 keV X-ray fluxes were obtained from the 14 – 195 keV or 15 – 50 keV *Swift*/BAT count rate, or 2–10 keV *Swift*/XRT fluxes. For 2004–2017, the 14–195 keV count rate was obtained from the 157-month catalog¹. From 2018, the 15 – 50 keV light curve was recovered from the BAT Hard X-ray transient monitor². The 2 – 10 keV fluxes were obtained from spectral analysis of 0.5 – 10 keV *Swift*/XRT observations. These count rates and fluxes were converted to 14 – 150 keV fluxes, assuming a power-law spectrum with $\Gamma = 1.8$ (Ricci et al. 2017).

The bolometric luminosity (L_{bol}) was calculated using Eddington ratio (λ_{Edd}) dependent bolometric correction factors ($\kappa_{14-195 \text{ keV}}$) of Gupta et al. (2024). According to this recent study, the bolometric correction factor is given by $\log \kappa_{14-195} = (0.13 \pm 0.04) \log \lambda_{\text{Edd}} + (1.04 \pm 0.05)$.

3. Results and discussions

3.1. Lightcurves

NGC 1566 showed an outburst in June 2018, when the fluxes in the optical, UV, IR, and X-ray bands increased, and the source moved from type 1.9 to type 1 spectral states (Oknyansky et al. 2019, 2020; Parker et al. 2019; Tripathi & Dewangan 2022). Figure 2 shows the light curves of NGC 1566 in 14 – 150 keV (*Swift*/BAT), 2 – 10 keV (*Swift*/XRT) and 230 GHz (ALMA) in the top, middle, and bottom panels, respectively, spanning the years 2014–2023.

The 2 – 10 keV X-ray and UVW2 flux increased about ~ 25 – 30 times during the outburst (Oknyansky et al. 2020; Jana et al. 2021). In optical, the ‘g’-band flux increased about $\sim 25\%$ compared to the pre-outburst phase (Kollatschny & Chelouche 2024). The flux also increased in the mid-infrared (MIR) band, where the fluxes in the W1 and W2 bands increased ~ 2.5 and ~ 4 times, respectively (see Section B). At this time, the mm flux was also observed to increase by a factor of ~ 2 ($\sim 9.8 \pm 1.0$ mJy). Later, in 2023, the mm flux decreased to $\sim 3.5 \pm 0.4$ mJy when the fluxes in other wavebands also decreased. Overall, we found that the mm continuum emission varies together with all the other bands during the CS event.

3.2. Relation between mm and X-ray emissions

Figure 3 displays the relation of the mm continuum flux at 230 GHz ($F_{230 \text{ GHz}}$) with the X-ray continuum flux at 14 – 150 keV ($F_{14-150 \text{ keV}}$). We find a possible positive correlation between $F_{230 \text{ GHz}}$ and $F_{14-150 \text{ keV}}$ with a Spearman correlation index of 0.54 and a p-value of 0.0168. A linear fit logarithmic space yields $\log F_{230 \text{ GHz}} = (0.39 \pm 0.13) \log F_{14-150 \text{ keV}} + (-10.62 \pm 1.34)$, with an intrinsic scatter of 0.05 dex (1σ level). While studying the relation between $\log L_{230 \text{ GHz}}$ and $\log L_{14-150 \text{ keV}}$ for 98 RQAGNs, Kawamuro et al. (2022) found a steeper slope, $\sim 1.19 \pm 0.08$ with a scatter of 0.30 dex. Similarly, Ricci et al. (2023) observed a slope of 1.22 ± 0.02 and an intrinsic scatter of 0.22 dex for the 100GHz mm emission ($L_{100 \text{ GHz}}$) and 14 – 150 keV X-ray flux in RQAGNs. Some portion of the scatter in the latter two studies could be attributed to non-simultaneous observations. The observed flatter slope in the current study could be attributed to extended or constant emission contaminating the weaker flux measurement.

¹ <https://swift.gsfc.nasa.gov/results/bs157mon/>

² <https://swift.gsfc.nasa.gov/results/transients/>

Figure 4 shows the relation between $F_{230 \text{ GHz}}/F_{14-150 \text{ keV}}$ and λ_{Edd} . The median of the ratio between mm and X-ray flux is found to be $\log(F_{230 \text{ GHz}}/F_{14-150 \text{ keV}}) = -4.42 \pm 0.21$. This result is consistent with the previous study of Kawamuro et al. (2022). The ratio is found to be somehow higher at low λ_{Edd} : for $\lambda_{\text{Edd}} < 10^{-2}$, the median ratio is found to be -4.01 ± 0.22 , while for $\lambda_{\text{Edd}} > 10^{-2}$ it is -4.52 ± 0.20 .

We did not observe any correlation between α_{mm} and the $F_{230 \text{ GHz}}$ (Figure 5). NGC 1566 generally showed a flat slope ranging between -0.3 ± 0.5 and 0.1 ± 0.4 , which indicates a compact optically thick source of mm emission (Rybicki & Lightman 1979).

3.3. Origin of the mm emission

3.3.1. Star formation and dust

Nuclear star formation (SF) can contribute to the mm emission through mechanisms such as free-free emission from H II Regions, synchrotron radiation from cosmic rays, or thermal dust emission (Condon 1992; Tabatabaei et al. 2017). The nuclear ($< 1''$) SF rate of NGC 1566 is estimated to be $5.3 \times 10^{-3} M_{\odot} \text{ yr}^{-1}$ (Smajić et al. 2015). We estimated the contribution of SF to the mm emission at 230 GHz due to the free-free and synchrotron emission using Equation 3 of Kawamuro et al. (2022). We obtained $L_{230 \text{ GHz}}^{\text{SFR}} \approx 5.6 \times 10^{33} \text{ erg s}^{-1}$ ($\approx 0.07 \mu\text{Jy}$), which is four orders of magnitude lower than the observed mm emission.

Thermal dust emission typically produces a steep spectral index ($\alpha_{\text{mm}} \sim 3.5$; Mullaney et al. 2011), which is inconsistent with the flat slope (-0.26 to 0.13) observed in NGC 1566. Furthermore, dust emission dominates at higher frequencies ($\nu > 300 \text{ GHz}$), making it unlikely to contribute significantly at 230 GHz (Barvainis et al. 1992; Hughes et al. 1993; Draine & Li 2007; Baskin & Laor 2021). At $\sim 230 \text{ GHz}$, expected free-free emission would be ~ 1 mJy, which is a few times less than the observed flux (Baskin & Laor 2021). Additionally, the free-free emission from a dusty torus and SF would not exhibit variability on the observed timescales (Baskin & Laor 2021).

3.3.2. Compact jet

A sub-parsec-scale unresolved jet could, in principle, contribute to the mm emission observed in NGC 1566 (e.g., Panessa et al. 2019). Compact jets are well studied in black hole X-ray binaries (BHXBs), where their presence and evolution are strongly tied to the accretion state of the system (Corbel et al. 2000; Fender & Belloni 2004; Russell et al. 2015; Tetarenko et al. 2021). In BHXBs, a steady, compact jet produces strong radio emission during the low-hard state, whereas in the high-soft state, the jet weakens, leading to a significant drop in radio flux (Fender & Belloni 2004; Jana et al. 2017; Tremou et al. 2020).

NGC 1566 is a CSAGN, which showed dramatic spectral transitions. The CSAGNs often show striking similarities in the spectral and timing properties with the BHXBs (Noda & Done 2018; Ruan et al. 2019; Jana et al. 2021). If a similar disk-jet coupling remains the same in CSAGNs, one would expect a decline in jet-related mm emission during high-accretion states, mirroring the behavior seen in BHXBs. However, in NGC 1566, the mm flux increases with the accretion activity, contradicting this expectation. This

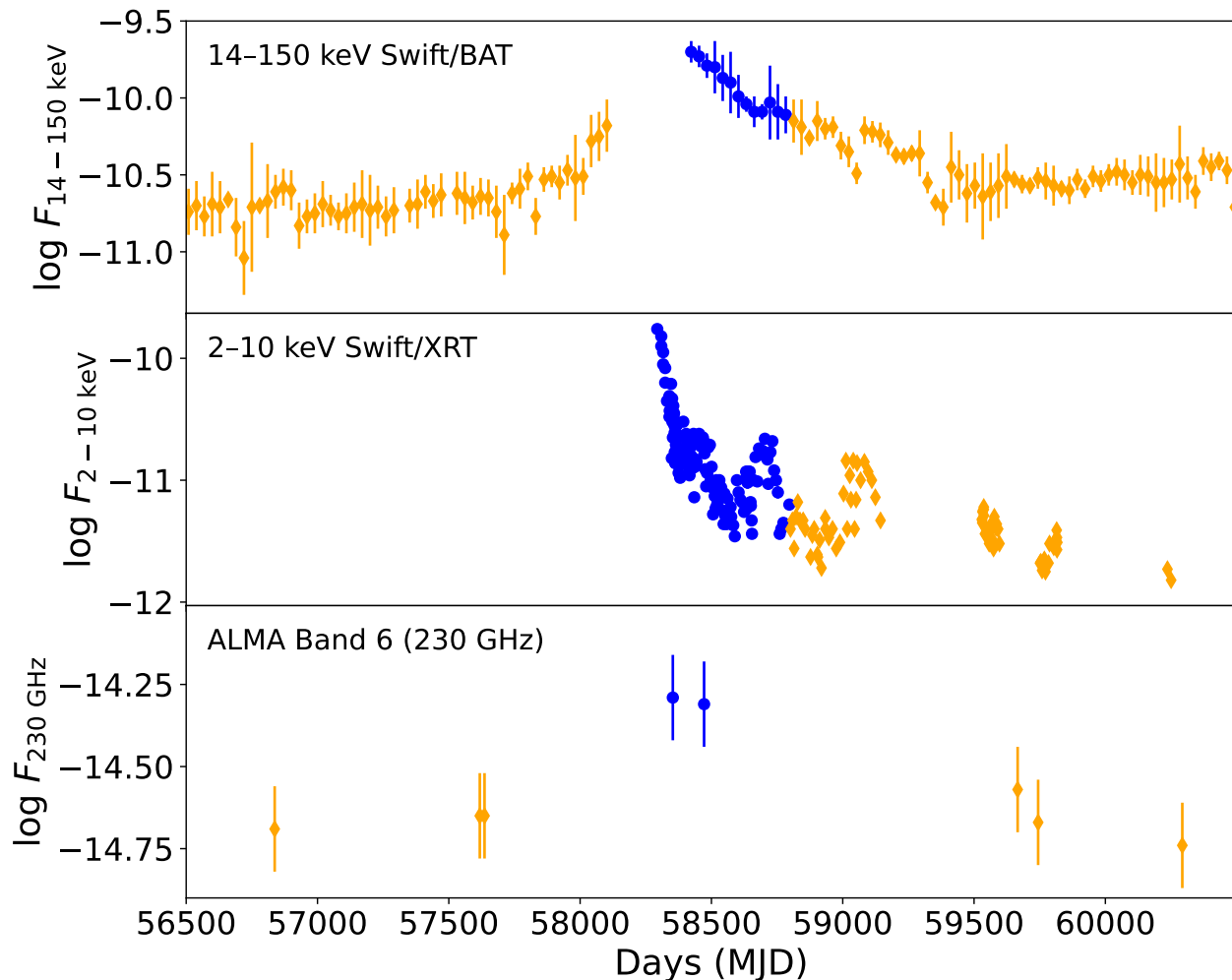


Fig. 2. Light curves of NGC 1566. Top panel: *Swift*/BAT flux (14 – 150 keV; $F_{14-150 \text{ keV}}$), middle panel: *Swift*/XRT flux ($F_{2-10 \text{ keV}}$; 2 – 10 keV), and bottom panel: ALMA band 6 flux (230 GHz; $F_{230 \text{ GHz}}$). The $F_{14-150 \text{ keV}}$, $F_{2-10 \text{ keV}}$ and $F_{230 \text{ GHz}}$ are in unit of $\text{erg cm}^{-2} \text{ s}^{-1}$. The blue circles and orange diamonds represent the data from type 1 and type 2 states, respectively. The *Swift*/BAT data are obtained from the BAT 157-month catalog and BAT hard X-ray transient monitor for two periods, until 2017 and after 2018, respectively. Due to unavailability of the data, there is a gap between January 2018 and December 2018 in the *Swift*/BAT lightcurve. The BAT data are binned over 30 days, while the XRT data correspond to single exposures.

indicates that compact jets are unlikely to be the primary contributor to the mm emission of NGC 1566.

3.3.3. Outflow driven shock

The AGN outflows can collide with the surrounding interstellar medium and produce shocks. The shock accelerates electrons, which in turn produce synchrotron emission (e.g., Hwang et al. 2018; Liao et al. 2024). It has been suggested that the ratio of synchrotron to AGN bolometric flux would be $\sim 10^{-5} - 10^{-6}$ if $\sim 0.5\% - 5\%$ of the bolometric luminosity is converted into the kinetic energy, and then $\sim 1\%$ of the outflow energy is used to produce relativistic particles that radiate synchrotron emission (Nims et al. 2015). In this case, the radio emission is expected to arise from a size of several 100 pc (Yamada et al. 2024).

Interestingly, we found a similar ratio between the mm and bolometric flux ($F_{230 \text{ GHz}} \sim 10^{-5} F_{\text{bol}}$) in NGC 1566. NGC 1566 showed X-ray wind with velocity, $v_{\text{out}} \sim 500 \text{ km s}^{-1}$ in the high accretion state (Parker et al. 2019). Conservatively assuming the outflow velocity as the escape veloc-

ity, we estimated the location of the outflow as $> 7 \times 10^{14} \text{ cm} \sim 2 \times 10^{-4} \text{ pc}$. The mass outflow rate can be estimated using $\dot{M}_{\text{out}} = \Omega m_p n_e v_{\text{out}} R^2$ (Krongold et al. 2007), where Ω is the covering factor of the wind, n_e is the electron density. Substituting, $N_{\text{H}} = nR$ in the above equation, we obtained, $\dot{M}_{\text{out}} = \Omega m_p n_e v_{\text{out}} R^2$, where $N_{\text{H}} \sim 2.5 \times 10^{20} \text{ cm}^{-2}$ (Parker et al. 2019). We estimated a conservative value of mass outflow rate as $\dot{M}_{\text{out}} \sim 2 \times 10^{19} \text{ g s}^{-1}$. This would correspond to a kinetic energy of $E_{\text{kin}} = 1/2 \dot{M}_{\text{out}} v_{\text{out}}^2 \sim 10^{34} \text{ erg s}^{-1}$ which translates to the flux of $\sim 2 \mu\text{Jy}$ at 230 GHz. This is lower by several orders than the observed continuum mm emission in NGC 1566.

3.3.4. Synchrotron emission in X-ray corona

A magnetized X-ray corona, heated by magnetic reconnection, can naturally produce mm emission via synchrotron radiation from relativistic non-thermal electrons (Di Matteo et al. 1997; Fabian et al. 2002; Laor & Behar 2008; Inoue & Doi 2014; Raginski & Laor 2016). The observed tight correlation between the mm and X-ray flux suggests

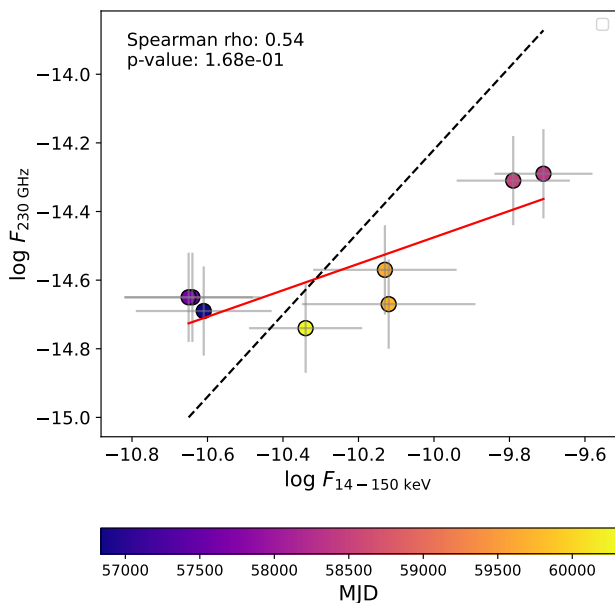


Fig. 3. Variation of the mm flux at 230 GHz ($F_{230 \text{ GHz}}$) as a function of 14–150 keV X-ray flux ($F_{14-150 \text{ keV}}$). The red solid line represent the best-fit. The black-dashed line represent $F_{230 \text{ GHz}} - F_{14-150 \text{ keV}}$ relation from Kawamuro et al. (2022).

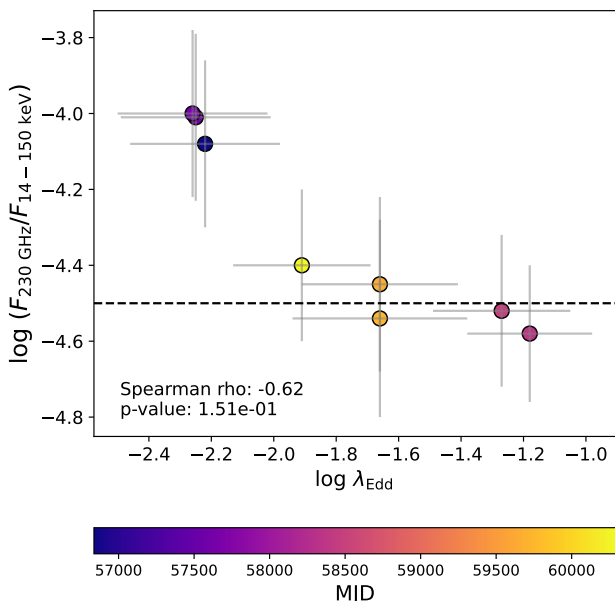


Fig. 4. Variation of the ratio of the mm flux to X-ray flux as a function of Eddington ratio. The horizontal dashed line represents the ratio of the mm flux to X-ray flux from Kawamuro et al. (2022).

that mm and X-ray emission could be coupled and originate in a similar region (Kawamuro et al. 2022; Ricci et al. 2023).

We find no correlation between α_{mm} and $F_{230 \text{ GHz}}$, which is consistent with and in agreement with the findings of Kawamuro et al. (2022). The observed α_{mm} suggests that the mm emission originates in an optically thick region. We calculated the size of the self-absorbed synchrotron source

as $R_{\text{mm}} \sim 4 - 7 \times 10^{-5} \text{ pc}$ or $\sim 100 - 200 R_g$, considering magnetic energy density is in equipartition with the photon energy density, and using Equation (22) of Laor & Behar (2008). The equipartition magnetic field (B_{eq}) is found in the range $\sim 100 - 300 \text{ G}$, which is higher than typical value of magnetic field (e.g., Inoue & Doi 2018). Considering magnetic field $B=10 \text{ G}$, as seen in IC 4329A (Inoue & Doi 2018, see also Inoue et al. 2020; Michiyama et al. 2023), the size of the mm emitting source would be $\sim 50 - 100 R_g$. The size of the X-ray corona (R_X) is estimated to be $R_X \sim 20 - 40 R_g$ from the broadband X-ray spectral study of NGC 1566 (Jana et al. 2021), using OPTXAGNF model (Done et al. 2012). This indicates the radio sphere may coincide with the X-ray corona or be slightly extended. Considering $R_X = R_{\text{mm}}$, we estimated the magnetic field in the range of $\sim 0.1 - 1 \text{ G}$. This is similar to the magnetic field found in lensed quasar RXJ J1131–1231, where the mm emitting region is constrained to be $< 46 R_g$ (Rybak et al. 2025). Recently, del Palacio et al. (2025) constructed radio to far infrared SED model for coronal mm emission to constrain the magnetic field and coronal size. By applying their model to seven RQAGNs, the authors found B in the range of $\sim 10 - 150 \text{ G}$, which is higher than our simple estimation. This suggests a detailed SED modeling is required to constrain the magnetic field in NGC 1566.

The enhancement of mm flux compared to the X-ray flux at low Eddington ratios (see Fig 4) can be attributed to two mechanisms: an increase in the non-thermal electron population or strengthening of the magnetic field (Inoue & Doi 2014). The observed constant spectral index (α_{mm} , Fig. 5) indicates minimal change in the electron energy distribution, suggesting cooling effects are not significant. This stability in α_{mm} makes substantial magnetic field variations unlikely. The observed possible anti-correlation of the mm to X-ray emission ratio with λ_{Edd} (Fig. 4) provides an interesting insight. Lower λ_{Edd} , which implies lower accretion densities, correspond to higher mm fluxes. This can be explained by the density dependence of particle acceleration efficiency – in lower-density flows, particles are more easily accelerated to non-thermal energies. Consequently, this could lead to a larger non-thermal electron population and enhanced mm emission. Further dense light curve data sets would test this scenario.

3.4. Implication of mm emission in NGC 1566

NGC 1566 underwent an outburst in 2018, transitioning to the type 1 state from the type 2 state (Oknyansky et al. 2019; Ochmann et al. 2024). Later in 2020, the source moved back to the type 2 state with the fluxes decreasing in all wavebands (Xu et al. 2024). The change in the accretion rate drives the CS transition in this source (Jana et al. 2021, 2025). The X-ray flux, which is considered to be a tracer of the accretion rate in AGN, is found to correlate with the UV, optical, and MIR emission (Oknyansky et al. 2019, 2020). The mm emission is also found to follow a similar trend as the UV, optical, MIR, and X-ray emission. The tight correlation between X-ray and mm emission in NGC 1566 suggests a strong link between mm emission and accretion activity.

A simple estimation indicates that the free-free emission from dust could contribute up to $\sim 1 \text{ mJy}$ at $\sim 230 \text{ GHz}$ in NGC 1566, making this contribution non-negligible (see Section 3.3.1). Despite this potential contamination, vari-

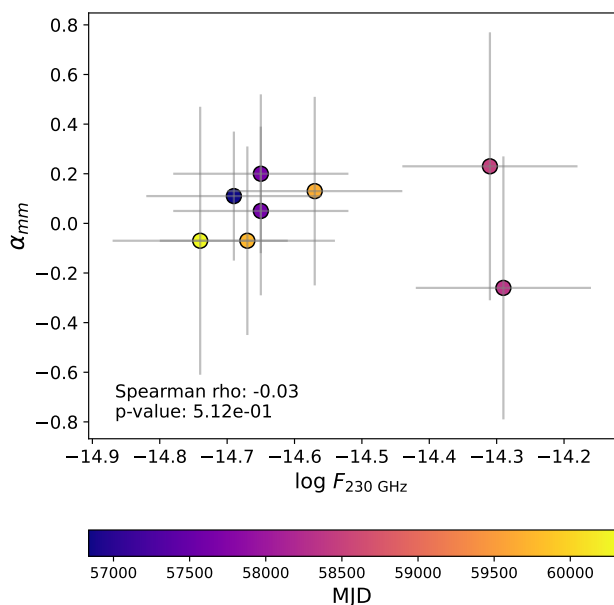


Fig. 5. Variation of in-band spectral index (α_{mm}) as a function of 230 GHz flux ($F_{230 \text{ GHz}}$). The red solid line shows the best-fit.

ous correlations between mm and X-ray emission indicate that the X-ray corona remains the dominant source of mm emission in NGC 1566. Our results confirm the idea that the mm emission can be used as a tracer of AGN activity in RQAGNs (see also, Kawamuro et al. 2022; Ricci et al. 2023).

4. Summary & Conclusions

In this work, we investigate the mm emission variability of CSAGN for the first time, providing new insights into its nature. Here, we studied NGC 1566 using archival high-resolution ($0''.3 - 7''.3$) ALMA observations in Band 6 (~ 230 GHz) taken in eight different epochs between 2014 and 2023. Our findings are the following:

1. We observed a strong correlation between mm and X-ray emission with an intrinsic scatter of 0.05 dex (1σ), suggesting they are energetically coupled and likely originate in a similar physical region.
2. We discuss several possible physical mechanisms that could be responsible for the bulk of the mm continuum emission in NGC 1566. We discard star formation, outflow-driven shock, and compact jet as possible contributors to the mm emission. The free-free emission from dust could contribute up to ~ 1 mJy in mm wavebands; however, this would be non-variable. Despite this, the X-ray corona is found to be a dominant contributor to the nuclear mm emission.
3. We did not observe any significant correlation between α_{mm} and $F_{230 \text{ GHz}}$, although a possible negative trend is seen. The observed α_{mm} suggests that the mm emission arises from a compact optically thick radio sphere, which could coincide with the X-ray corona.
4. The median of $\log(F_{230 \text{ GHz}}/F_{14-150 \text{ keV}})$ is found to be -4.42 ± 0.21 . While no strong correlation was found between the flux ratio and λ_{Edd} , the ratio appears higher in the low-accretion state. This could be due to more

5. The mm emission follows a similar trend as the X-ray, UV, optical, and MIR wavebands. Along with the strong mm-X-ray correlation, this suggests a close connection between mm emission and the accretion rate. These findings support the use of mm emission as a tracer of accretion activity in radio-quiet AGNs.

Our findings indicate that the compact X-ray corona is the most probable source of mm-wave emission in NGC 1566. Future studies will focus on observing the source across different accretion states using simultaneous multi-wavelength data, including radio, mm, optical, and X-ray bands. Long-term monitoring campaigns in the mm-wave band will be crucial for capturing transient phenomena and understanding the connection between mm-wave emission and changes in the accretion flow. It will also help us to understand the radio emission in RQAGNs, as well as the heating mechanism of the X-ray corona.

Acknowledgements. We thank the reviewer E. Behar for his invaluable comments and suggestions that improved the paper significantly. We acknowledge support from ANID grants FONDECYT Postdoctoral fellowship 3230303 (AJ), Fondecyt Regular grant 1230345 (CR) and 1241005 (FEB), ANID BASAL project FB210003 (CR, FEB), the China-Chile joint research fund (CR), and the Millennium Science Initiative, AIM23-0001 (FEB). YI is supported by NAOJ ALMA Scientific Research Grant Number 2021-17A; JSPS KAKENHI Grant Number JP22K18277; and World Premier International Research Center Initiative (WPI), MEXT, Japan. TK is supported by JSPS KAKENHI 23K13153. BT is supported by the European Research Council (ERC) under the European Union’s Horizon 2020 research and innovation program (grant agreement number 950533). This paper makes use of the following ALMA data: ADS/JAO.ALMA#2012.1.00474.S, ADS/JAO.ALMA#2015.1.00925.S, ADS/JAO.ALMA#2017.1.00392.S, ADS/JAO.ALMA#2018.1.01651.5, ADS/JAO.ALMA#2021.1.01150.S, ADS/JAO.ALMA#2023.1.01182.S. ALMA is a partnership of ESO (representing its member states), NSF (USA) and NINS (Japan), together with NRC (Canada), NSTC and ASIAA (Taiwan), and KASI (Republic of Korea), in cooperation with the Republic of Chile. The Joint ALMA Observatory is operated by ESO, AUI/NRAO and NAOJ.

DATA AVAILABILITY

All the data used in the paper are publicly available.

References

- Alloin, D., Pelat, D., Phillips, M. M., Fosbury, R. A. E., & Freeman, K. 1986, *ApJ*, 308, 23
- Baldi, R. D., Behar, E., Laor, A., & Horesh, A. 2015, *MNRAS*, 454, 4277
- Baribaud, T., Alloin, D., Glass, I., & Pelat, D. 1992, *A&A*, 256, 375
- Barvainis, R., Antonucci, R., & Coleman, P. 1992, *ApJ*, 399, L19
- Baskin, A. & Laor, A. 2021, *MNRAS*, 508, 680
- Begelman, M. C., Blandford, R. D., & Rees, M. J. 1984, *Reviews of Modern Physics*, 56, 255
- Behar, E., Baldi, R. D., Laor, A., et al. 2015, *MNRAS*, 451, 517
- Behar, E., Kaspi, S., Paubert, G., et al. 2020, *MNRAS*, 491, 3523
- Behar, E., Vogel, S., Baldi, R. D., Smith, K. L., & Mushotzky, R. F. 2018, *MNRAS*, 478, 399
- Beloborodov, A. M. 2017, *ApJ*, 850, 141
- Chakrabarti, S. & Titarchuk, L. G. 1995, *ApJ*, 455, 623
- Cheng, H., Liu, B. F., Liu, J., et al. 2020, *MNRAS*, 495, 1158
- Condon, J. J. 1992, *ARA&A*, 30, 575

- Corbel, S., Fender, R. P., Tzioumis, A. K., et al. 2000, *A&A*, 359, 251
- del Palacio, S., Yang, C., Aalto, S., et al. 2025, arXiv e-prints, arXiv:2504.07762
- Di Matteo, T., Celotti, A., & Fabian, A. C. 1997, *MNRAS*, 291, 805
- Done, C., Davis, S. W., Jin, C., Blaes, O., & Ward, M. 2012, *MNRAS*, 420, 1848
- Draine, B. T. & Li, A. 2007, *ApJ*, 657, 810
- Ehle, M., Beck, R., Haynes, R. F., et al. 1996, *A&A*, 306, 73
- Elagali, A., Staveley-Smith, L., Rhee, J., et al. 2019, *MNRAS*, 487, 2797
- Evans, P. A., Beardmore, A. P., Page, K. L., et al. 2009, *MNRAS*, 397, 1177
- Fabian, A. C., Ballantyne, D. R., Merloni, A., et al. 2002, *MNRAS*, 331, L35
- Fabian, A. C., Lohfink, A., Kara, E., et al. 2015, *MNRAS*, 451, 4375
- Fender, R. & Belloni, T. 2004, *ARA&A*, 42, 317
- Field, G. B. & Rogers, R. D. 1993, *ApJ*, 403, 94
- Gupta, K. K., Ricci, C., Temple, M. J., et al. 2024, arXiv e-prints, arXiv:2409.12239
- Haardt, F. & Maraschi, L. 1993, *ApJ*, 413, 507
- Hopkins, P. F. 2024, arXiv e-prints, arXiv:2407.00160
- Hughes, D. H., Robson, E. I., Dunlop, J. S., & Gear, W. K. 1993, *MNRAS*, 263, 607
- Hunter, T. R., Indebetouw, R., Brogan, C. L., et al. 2023, *PASP*, 135, 074501
- Hwang, H.-C., Zakamska, N. L., Alexandroff, R. M., et al. 2018, *MNRAS*, 477, 830
- Inoue, Y. & Doi, A. 2014, *PASJ*, 66, L8
- Inoue, Y. & Doi, A. 2018, *ApJ*, 869, 114
- Inoue, Y., Khangulyan, D., & Doi, A. 2020, *ApJ*, 891, L33
- Inoue, Y., Takasao, S., & Khangulyan, D. 2024, *PASJ*, 76, 996
- Jana, A., Chakrabarti, S. K., & Debnath, D. 2017, *ApJ*, 850, 91
- Jana, A., Kumari, N., Nandi, P., et al. 2021, *MNRAS*, 507, 687
- Jana, A., Ricci, C., Temple, M. J., et al. 2025, *A&A*, 693, A35
- Kawamuro, T., Ricci, C., Imanishi, M., et al. 2022, *ApJ*, 938, 87
- Kollatschny, W. & Chelouche, D. 2024, *A&A*, 690, L2
- Koss, M. J., Ricci, C., Trakhtenbrot, B., et al. 2022, *ApJS*, 261, 2
- Krongold, Y., Nicastro, F., Elvis, M., et al. 2007, *ApJ*, 659, 1022
- Laor, A. & Behar, E. 2008, *MNRAS*, 390, 847
- Liao, M., Wang, J., Ren, W., & Zhou, M. 2024, *MNRAS*, 528, 3696
- MacLeod, C. L., Ross, N. P., Lawrence, A., et al. 2016, *MNRAS*, 457, 389
- Merloni, A., Dwelly, T., Salvato, M., et al. 2015, *MNRAS*, 452, 69
- Merloni, A. & Fabian, A. C. 2001, *MNRAS*, 321, 549
- Michiyama, T., Inoue, Y., & Doi, A. 2023, *PASJ*, 75, 874
- Michiyama, T., Inoue, Y., Doi, A., et al. 2024, *ApJ*, 965, 68
- Mullaney, J. R., Alexander, D. M., Goulding, A. D., & Hickox, R. C. 2011, *MNRAS*, 414, 1082
- Nims, J., Quataert, E., & Faucher-Giguère, C.-A. 2015, *MNRAS*, 447, 3612
- Noda, H. & Done, C. 2018, *MNRAS*, 480, 3898
- Ochmann, M. W., Kollatschny, W., Probst, M. A., et al. 2024, *A&A*, 686, A17
- Oknyansky, V. L., Brotherton, M. S., Tsygankov, S. S., et al. 2021, *MNRAS*, 505, 1029
- Oknyansky, V. L., Winkler, H., Tsygankov, S. S., et al. 2020, *MNRAS*, 498, 718
- Oknyansky, V. L., Winkler, H., Tsygankov, S. S., et al. 2019, *MNRAS*, 483, 558
- Padovani, P. 2017, *Nature Astronomy*, 1, 0194
- Panessa, F., Baldi, R. D., Laor, A., et al. 2019, *Nature Astronomy*, 3, 387
- Parker, M. L., Schartel, N., Grupe, D., et al. 2019, *MNRAS*, 483, L88
- Petrucci, P. O., Piétu, V., Behar, E., et al. 2023, *A&A*, 678, L4
- Raginski, I. & Laor, A. 2016, *MNRAS*, 459, 2082
- Reis, R. C. & Miller, J. M. 2013, *ApJ*, 769, L7
- Ricci, C., Chang, C.-S., Kawamuro, T., et al. 2023, *ApJ*, 952, L28
- Ricci, C., Kara, E., Loewenstein, M., et al. 2020, *ApJ*, 898, L1
- Ricci, C. & Trakhtenbrot, B. 2023, *Nature Astronomy*, 7, 1282
- Ricci, C., Trakhtenbrot, B., Koss, M. J., et al. 2017, *ApJS*, 233, 17
- Ruan, J. J., Anderson, S. F., Eracleous, M., et al. 2019, *ApJ*, 883, 76
- Russell, T. D., Miller-Jones, J. C. A., Curran, P. A., et al. 2015, *MNRAS*, 450, 1745
- Rybak, M., Sluse, D., Gupta, K. K., et al. 2025, arXiv e-prints, arXiv:2503.13313
- Rybicki, G. B. & Lightman, A. P. 1979, *Radiative processes in astrophysics* (Wiley, New York)
- Shablovinskaya, E., Ricci, C., Chang, C. S., et al. 2024, *A&A*, 690, A232
- Smajčić, S., Moser, L., Eckart, A., et al. 2015, *A&A*, 583, A104
- Stern, D., McKernan, B., Graham, M. J., et al. 2018, *ApJ*, 864, 27
- Tabatabaei, F. S., Schinnerer, E., Krause, M., et al. 2017, *ApJ*, 836, 185
- Temple, M. J., Ricci, C., Koss, M. J., et al. 2023, *MNRAS*, 518, 2938
- Tetarenko, A. J., Casella, P., Miller-Jones, J. C. A., et al. 2021, *MNRAS*, 504, 3862
- Trakhtenbrot, B., Arcavi, I., MacLeod, C. L., et al. 2019, *ApJ*, 883, 94
- Tremou, E., Corbel, S., Fender, R. P., et al. 2020, *MNRAS*, 493, L132
- Tripathi, P. & Dewangan, G. C. 2022, *ApJ*, 930, 117
- Wilson, A. S. & Colbert, E. J. M. 1995, *ApJ*, 438, 62
- Xu, D. W., Komossa, S., Grupe, D., et al. 2024, *Universe*, 10, 61
- Yamada, T., Sakai, N., Inoue, Y., & Michiyama, T. 2024, *ApJ*, 968, 116
- Yuan, F. & Narayan, R. 2014, *ARA&A*, 52, 529
- Zelty, G., Trakhtenbrot, B., Eracleous, M., et al. 2024, *ApJ*, 966, 85

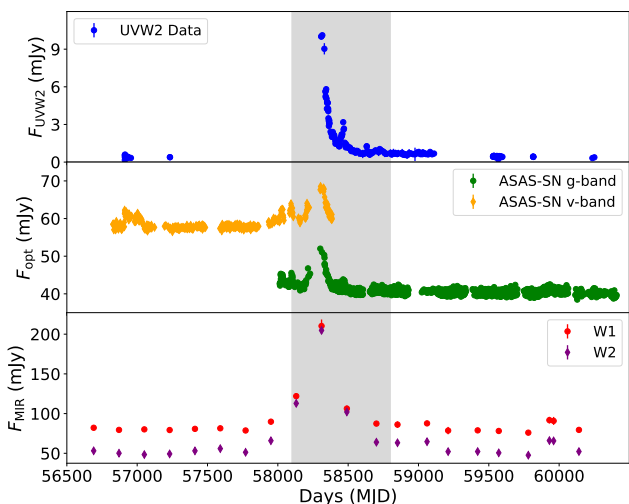


Fig. B.1. Lightcurves of NGC 1566. Top panel: UV flux from *Swift*/UVOT in UVW2 band (F_{UVW2}). Middle panel: optical flux (F_{opt}) from ASSAS-Sn. The orange diamonds and green circles represent the lightcurve in ‘v’ and ‘g’ band, respectively. Bottom panel: Mid-infrared fluxes (F_{MIR}), obtained from WISE and NEOWISE. The red circles and purple diamonds represent the lightcurve in W1 and W2 bands, respectively.

Appendix A: Observation log

Appendix B: Multi-wavelength observations

The *Swift*/UVW2 photometric flux was estimated using UVOTSOURCE task. The AGN flux was estimated by subtracting the host galaxy contribution in the UVW2 band. The host galaxy flux was taken from Gupta et al. (2024). We obtained mid-infrared (MIR) lightcurves from WISE in W1 ($3.4 \mu\text{m}$) and W2 ($4.6 \mu\text{m}$) band from IPAC. We also obtained optical lightcurves in g and v band from ASSAS-Sn archive³. Figure B.1 shows the lightcurve in UVW2, optical (v and g-band) and MIR wavebands.

Appendix C: ALMA data reduction

We utilized archival ALMA band-6 observations, which was obtained in eight epochs. The data were calibrated using python script `scriptForPI.py` in appropriate CASA version. Once the data were calibrated, and measurement set (MS) was generated, we used CASA 6.5.4.9 for the following tasks. First, using CASA task `tclean`, we generated clean images with appropriate cell sizes with weighting = briggs (robust=0.5) and original beam sizes. We used all the spectral windows to generate each clean image. With the same process, the clean images for individual spectral windows are also generated, which we used to calculate the spectral index (α_{mm}).

In order to maintain consistency of the spatial resolution across the different epochs, we made their final clean images with a same beam size of $7.31'' \times 4.96''$, which represents the lowest resolution observations. We found the fluxes with the original beam size are within $\sim 5\%$ of the ones with the beam size of $7.3'' \times 4.96''$. Hence, we used the fluxes obtained from the original beam size in the paper. Figure C.1 shows the variation of 230 GHz peak flux

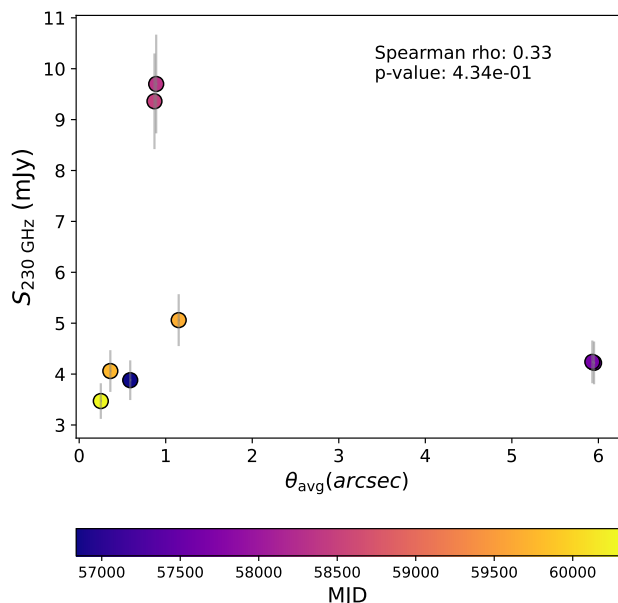


Fig. C.1. Variation of the peak flux density ($S_{230 \text{ GHz}}$) with average beam size (θ_{avg}).

density ($S_{230 \text{ GHz}}$) with the average beam size (θ_{avg}). The average beam size is calculated as $\theta_{avg} = \sqrt{\theta_{major} \times \theta_{minor}}$. The observed flux is independent of the beam size, indicating our result is not affected by the different beam sizes.

Appendix D: X-ray data analysis

The 2 – 10 keV fluxes were estimated by analyzing 0.5 – 10 keV *Swift*/XRT spectra, processed using the UK Swift Science Data Centre tools (Evans et al. 2009). Spectra were modeled in XSPEC as $TBABS\text{Gal} \times ZPHABS \times (BB+POWERLAW)$, where $TBABS\text{Gal}$ and $ZPHABS$ account for Galactic and intrinsic absorption, and the $DISKBB$ and $POWERLAW$ components represent soft-excess and Comptonized emission, respectively.

³ <https://asas-sn.osu.edu/photometry>

Table A.1. Details of the ALMA Observations

Epoch	Project code	ν_{cen} (GHz)	Date (yyyy-dd-mm)	Date (MJD)	$\theta_{\text{beam}}^{\text{maj}} \times \theta_{\text{beam}}^{\text{min}}$ (arcsec)	$\theta_{\text{beam,pc}}^{\text{maj}} \times \theta_{\text{beam,pc}}^{\text{min}}$ (pc)	S_{ν}^{peak}	$S_{\nu,7.31'' \times 4.96''}^{\text{peak}}$	SNR
(1)	(2)	(3)	(4)	(5)	(6)	(7)	(8)	(9)	(10)
1	2012.1.00474.S	235.37	2014-06-29	56837	0.63×0.55	55×48	3.90	3.69	177
2	2015.1.00925.S	223.81	2016-08-18	57618	7.31×4.85	636×422	3.91	4.17	333
3	2015.1.00925.S	223.79	2016-09-05	57636	7.08×4.96	616×432	4.22	4.32	313
4	2017.1.00392.S	223.63	2018-08-23	58353	1.04×0.77	90×67	9.77	10.88	579
5	2018.1.01651.5	223.66	2018-12-20	58472	0.96×0.79	84×69	9.30	10.54	705
6	2021.1.01150.S	234.82	2022-03-28	59666	1.24×1.07	108×93	5.07	5.20	256
7	2021.1.01150.S	234.82	2022-06-14	59744	0.44×0.29	38×25	4.05	4.36	226
8	2023.1.01182.S	224.93	2023-12-15	60293	0.27×0.23	23×20	3.48	3.65	171

Note: (1) Epoch of observation, (2) ALMA project code, (3) central frequency in GHz, (4) and (5) observation date in yyyy-mm-dd and MJD unit respectively. (6) Beam size in unit of arcseconds along major and minor axes, (7) physical beam size in unit of parsecs along major and minor axes, (8) peak flux density with original beam size in mJy beam⁻¹, (9) peak flux density with 7.31'' × 4.96'' beam size in mJy beam⁻¹, (10) signal-to-noise ratio of the detection. We used 10% uncertainties for flux density in all epochs.

Table A.2. Important physical parameters

Epoch	$\log F_{230 \text{ GHz}}$ (erg cm ⁻² s ⁻¹)	$\log F_{14-150 \text{ keV}}$ (erg cm ⁻² s ⁻¹)	$\log(\frac{F_{230 \text{ GHz}}}{F_{14-150 \text{ keV}}})$	$\log \lambda_{\text{Edd}}$	α_{mm}	R_{mm} (10 ⁻⁵ pc)	R_{mm} (R_{g})	B_{eq} (G)
(1)	(2)	(3)	(4)	(5)	(6)	(7)	(8)	(9)
1	-14.69 ± 0.13	-10.61 ± 0.18	-4.08 ± 0.22	-2.22 ± 0.24	0.11 ± 0.26	3.84	117	143
2	-14.65 ± 0.13	-10.64 ± 0.18	-4.01 ± 0.22	-2.25 ± 0.24	0.05 ± 0.34	3.93	120	133
3	-14.65 ± 0.13	-10.65 ± 0.17	-4.00 ± 0.22	-2.26 ± 0.24	0.20 ± 0.32	3.94	120	132
4	-14.29 ± 0.13	-9.71 ± 0.13	-4.58 ± 0.18	-1.18 ± 0.20	-0.26 ± 0.53	7.03	214	257
5	-14.31 ± 0.13	-9.79 ± 0.15	-4.52 ± 0.20	-1.27 ± 0.22	0.23 ± 0.54	6.78	206	240
6	-14.57 ± 0.13	-10.13 ± 0.19	-4.45 ± 0.23	-1.66 ± 0.25	0.13 ± 0.38	4.84	147	213
7	-14.67 ± 0.13	-10.12 ± 0.23	-4.54 ± 0.26	-1.66 ± 0.28	-0.07 ± 0.38	4.44	135	234
8	-14.74 ± 0.13	-10.34 ± 0.15	-4.40 ± 0.20	-1.91 ± 0.22	-0.07 ± 0.54	3.94	120	198

Note: (1) epochs, (2) and (3) 230 GHz and 14 – 150 keV flux in unit of erg cm⁻² s⁻¹, respectively. (4) Ratio of mm flux to X-ray flux, (5) Eddington ratio, (6) in-band spectral index, (7) and (8) size of mm emitting region in 10⁻⁵ pc and R_{g} , respectively. (9) Equipartition magnetic field in Gauss.